Energy, Environmental, and Catalysis Applications

A direct Z-scheme g-C3N4/FeWO4 nanocomposite for Enhanced and Selective Photocatalytic CO2 Reduction under Visible Light

Reshma Bhosale, Srashti Jain, Chathakudath Prabhakaran Vinod, Santosh Kumar, and Satishchandra Ogale

ACS Appl. Mater. Interfaces, **Just Accepted Manuscript** • DOI: 10.1021/acsami.8b22434 • Publication Date (Web): 25 Jan 2019

A Direct Z-scheme g-C_3N_4/$FeWO_4$ Nanocomposite for Enhanced and Selective Photocatalytic CO_2 Reduction Under Visible Light

Reshma Bhosale, [a] Srashti Jain,[a] Chathakudath Prabhakaran Vinod, [b] Santosh Kumar, [c*] and Satishchandra Ogale [a*]

[a]Department of Physics and Centre for Energy Science, Indian Institute of Science Education and Research (IISER), Pune 411008, India.

[b]Catalysis Division, CSIR-National Chemical Laboratory, Dr. Homi Bhabha Road, Pune 411 008, India.

[c]Department of Chemical Engineering, University of Bath, Claverton, Bath, BA2 7AY, United Kingdom.

***Corresponding Author**

Email: satishogale@gmail.com, S.Kumar@bath.ac.uk

ABSTRACT

Photocatalytic reduction of CO_2 to renewable solar fuels is considered to be the promising strategy to simultaneously solve both the global warming and energy crises. However, development of superior photocatalytic system with high product selectivity for CO_2 reduction under solar light is the prime requisite. Herein, a series of nature-inspired Z-scheme g C_3N_4/$FeWO_4$ composites are prepared for higher performance and selective CO_2 reduction to CO as solar fuel under solar light. The novel direct Z-scheme coupling of the visible light active $FeWO_4$ nanoparticles with C_3N_4 nanosheets is seen to exhibit excellent performance for CO production with a rate of 6 μmol/g/hr at ambient temperature, almost 6 times higher compared to pristine C_3N_4 and 15 times higher than pristine $FeWO_4$.More importantly, selectivity for CO is 100% over other carbon products from CO2reduction and more than 90% over H_2 product from water splitting. Our results clearly demonstrate that the staggered band structure between $FeWO_4$ and C_3N_4

reflecting nature-inspired Z-scheme system not only favors superior spatial separation of electron-hole pair in g-C_3N_4/$FeWO_4$, but also shows good reusability. The present work provides unprecedented insights for constructing the direct Z-scheme by mimicking nature for high performance and selective photocatalytic CO_2 reduction into solar fuels under solar light.

KEYWORDS: Photocatalysis, CO_2 reduction, solar fuels, C_3N_4, $FeWO_4$, Z scheme

1. INTRODUCTION:

Green-house effect and global warming are the most menacing concerns for the 21st century modern civilization, posing major challenges to the whole scientific community. With increase in the energy demand the consumption of fossil fuels has increased dramatically, contributing huge amounts of anthropogenic CO_2 emissions to the atmosphere and leading to environmental crisis.[1,2,3]Amongst the different potential solutions being considered, the use of abundantly available solar energy for CO_2 reduction to value added chemicals and/or fuels is considered to be the most attractive method to simultaneously solve both the energy and environmental problems.[3,4,5]However,the high thermodynamic stability and inertness of CO_2 with C=O bond dissociation energy of ~ 750 kJ/mol, which is higher than the other chemical bonds such as C-H (~430 kJ/mol) and C-C (~ 336 kJ/mol), necessitates high energy inputs for

the CO_2 conversions.[3,6,7] Although a number of solar active catalysts have been developed and examined for CO_2 photoreduction, most of them continue to suffer from one or more of the negativities such as low energy conversion efficiency, selectivity, instability, and incapability to suppress the competing HER reaction. Therefore, the design and development of highly active photocatalyst with product selectivity is still a grand challenge.

In recent years, organic polymeric photocatalyst, graphitic carbon nitride (g-C_3N_4) has emerged as a sustainable, cost effective, and environmental friendly visible light active semiconductor with suitable band gap of 2.6-2.8 eV. More importantly, g-C_3N_4 has relatively more negative conduction band potential w.r.t. to the CO_2 reduction potential, which demonstrates its high suitability for photocatalytic CO_2 reduction into wide range of value added chemicals and fuels such as CO, CH_4, and CH_3OH.[8,9] Despite its appropriate band-structure however, the photocatalytic efficiency still remains low due to the rapid recombination of photogenerated electrons and holes before they could participate in the surface reactions.[9,10] In order to slow down the recombination, several interesting strategies have been devised to improve the overall performance of g-C_3N_4.[11,12,13,14,15,16,17,18,19] Among them, coupling of C_3N_4 with other semiconductors with suitable band structure has proved to be an effective pathway to increase the life time of photogenerated charge carriers through the spatial separation of electrons and holes within the interfacial area. For example, Peng *et al*,[18] reported novel coupling of ZnO with

C_3N_4 for selective photoreduction of CO_2 to CH_3OH. Similarly, Xu *et al* [19] illustrated the improved charge separation in C_3N_4 by coupling of SnS_2 for enhanced photocatalytic CO_2 reduction to CH_4 and CH_3OH.Although, there are many such reports on coupling C_3N_4 with both large band gap, (ZnO[18,20] and TiO_2 [21,22]) and low band gap (In_2O_3,$NaNbO_3$,Ag_3PO_4 and SnS_2) [23,24,25,19]semiconductors for photocatalytic CO_2 reduction, achieving high efficiency and product selectivity still remains elusive. In coupling methodology, the nature-inspired Z-scheme mechanism has also been a more effective strategy as the photogenerated electrons with high reduction ability is restored in one photocatalyst whereas holes with high oxidizing ability are restored in other photocatalyst of photosystem, which are subsequently utilized for respective surface reactions.[26,27] Thus, superior charge separation and in turn high photocatalytic yield along with selectivity of products is achieved. Unfortunately, thus far, these systems are mostly examined for their application to photocatalytic water splitting or pollutant degradation.[28,29,30,31,32,33,34]Moreover, most of the existing Z-schemes have employed an additional sacrificial mediator, so-called indirect Z-scheme mechanism. [25,35,36]Therefore,for a scalable photocatalytic system with C_3N_4, developing a direct Z-scheme heterostructured material with suitable band-structure match is highly sought so as to achieve efficient spatial separation of charge carriers and thereby high performance as well as product selectivity.

With the current interesting and challenging scenario as a prerequisite, herein we introduce a new direct Z-scheme photocatalyst comprising $FeWO_4$ (band gap of 1.8-2.5 eV) [37,38] and C_3N_4 (band gap of 2.5-2.8 eV) [8,9] with highly suitable staggered band-structure for efficient and selective CO_2 photoreduction to CO under visible light.$FeWO_4$ was chosen particularly due to its visible light responsive nature, and most importantly its relatively negative conduction band potential (0.4 V – 0.7 V vs NHE) [39,40] w.r.t. to the C_3N_4 valence band potential. In principle, Ferrous Tungstate $FeWO_4$ belongs to fascinating family of wolframite type which has attracted tremendous attention due to its various technological applications in scintillators,[41] optical fibres,[28] sensors,[43] and catalysis [44,45,46,47].So far, $FeWO_4$ is not investigated much in the field of photocatalysis. Few reports on photocatalytic dye degradation such as methyl orange,[38] methylene blue,[37,40] Rhodamine B [48] and 4-nitrophenol [40] have appeared. In the present work, $FeWO_4$ was successfully coupled with C_3N_4 by simple wet chemical method as an efficient photocatalyst for the direct Z scheme without utilization of any mediator for photoreduction of CO_2 to CO. The obtained Z-scheme nanocomposite g-C_3N_4/$FeWO_4$ exhibited 6-fold and 15-fold enhancement in selective photocatalytic CO_2 reduction to CO over C_3N_4 and $FeWO_4$, respectively. Moreover, CO selectivity shown by this Z scheme photocatalyst is 100% over C_1 and other higher hydrocarbons and almost ~ 91% over the undesired H_2 evolution from water splitting. Our results clearly show that the direct Z scheme mechanism with staggered band structure of $FeWO_4$ band potential with C_3N_4 band edges favors superior charge separation of electron-hole pair in C_3N_4 and restores its reduction

ability leading to enhanced photocatalytic activity. Moreover, to best of our knowledge, $FeWO_4$ based materials have not been reported as CO_2 reduction photocatalyst till date.

2. EXPERIMENTAL SECTION:

2.1. Material Synthesis

a) Synthesis of C_3N_4: C_3N_4 was synthesized by following the protocol given in previously reported literature.[49] Briefly, Melamine ($C_3N_3(NH_2)_3$ (S D Fine Chem Limited) and NH_4Cl (Loba chemie) were mixed in 1:3 ratio by weight and ground properly in motor pestle. This mixture was heated in inert atmosphere at 550 °C for 4 h with 5°C/min in alumina boat. The sample was cooled down to room temperature and the obtained pale yellow coloured C_3N_4 powder was collected for further use.

b) Synthesis of $FeWO_4$: Simple hydrothermal route was used to synthesize $FeWO_4$ nanoparticles. 2mmol of Sodium Tungstate [$Na_2WO_4.2H_2O$, Loba chemie] and 2 mmol of Ferrous Ammonium Sulfate [$(NH_4)_2$ Fe $(SO_4)_2 \cdot 6H_2O$,] (FAS, Rankem) was separately dissolved in 25 ml of distilled water. FAS solution was added dropwise to the sodium tungstate solution with continuous stirring. The pH of the obtained solution was adjusted to 8 by adding a few drops of aq. NaOH solution. The overall mixture was transferred to 100 ml Teflon lined autoclave and kept for 12 h at 180°C. The final product thus obtained was washed thrice with distilled water and kept overnight for drying at 60°C.

c) Synthesis of $C_3N_4/FeWO_4$ composites: For preparing the 80% composite, 80 mg of C_3N_4 and 20mg of $FeWO_4$were dispersed in 10 ml of distilled water separately and sonicated for an hour to get well dispersed homogenous suspensions. Then, the two solutions were mixed and sonicated for the next 2hrs. The mixed solution was dried overnight at 80°C.The obtained powder was collected and heated in Ar at 400°C for 2h with 5°C/ min in alumina boat. Finally, the composite sample was cooled down to room temperature and collected. Similar method was used for 50% and 30% composites with respective C_3N_4 and $FeWO_4$ weight ratios.

2.2. Characterization:

Material Characterization: The structural phases of samples C_3N_4, $FeWO_4$ and $C_3N_4/FeWO_4$ were confirmed by X-ray diffraction (Bruker D8 Advance X-ray diffractometer equipped with Cu K_α lamp source for irradiation 1.54 Å). For the morphology study Field Emission Scanning Electron Microscopy (FESEM, FEI NOVA NANO SEM) and High-Resolution Transmission Electron Microscopy (HRTEM) (JEOL JEM-2200FS, from JEOL, Japan at an acceleration voltage of 200 keV) techniques were used. For surface area and porosity estimation, measurements were performed on Quantochrome Autosorb automated gas sorption analyser at 77 K. Fourier Transform Infrared Spectroscopy (FTIR) was performed on Thermo scientific NICOLET 6700 FTIR spectrophotometer in the range of 250-4000 cm^{-1} with $BaSO_4$ pellet as reference. Photoluminescence (PL) spectra of the samples were recorded at room temperature on

steady state spectroflurometer FLS 980 (Edinburgh Instruments) equipped with 450 W Xenon lamp. The Ultraviolet-Visible diffuse reflectance spectrum (UV−VIS DRS) was obtained by using SHIMADZU UV-3600 plus UV-VIS-NIR spectrophotometer with integrating sphere attachment.The X-ray Photoelectron Spectroscopy (XPS) measurement was carried out using Thermo Kalpha+ spectrometer using micro focused and monochromated Al K_α radiation with energy 1486.6 eV.

2.3 Photoelectrochemical Measurements: The on-off transient measurements were carried out in a three electrode system using AUTOLAB PGSTAT 30 potentiostat under the illumination of solar simulator (Newport) with UV (λ >420 nm) cut off filter and 100mW/cm^2 power density. Ag/AgCl was used as the reference electrode, and platinium as the counter electrode. The sample coated on Fluorine doped Tin oxide (FTO) served as the working electrode. The electrolyte used was 0.5 M Na_2SO_3.The photoelectrodes were fabricated by preparing the slurry in mortar pestal by adding 40 mg sample, 200 µl Nafion (5%) and 1ml iso-propanol (IPA). The obtained paste was coated on FTO with 1cm^2 area and heated at 250°C for 1hr to get homogenous film. Mott Schottky plots were recorded at a scan rate of 10mV/s in Na_2SO_3 neutral solution in dark at a frequency of 10 KHz.

2.4 Photocatalytic measurements: Photocatalytic CO_2 reduction experiments were carried out in stainless-steel photoreactor with quartz window set-up under the illumination of solar simulator (100 mW/cm^2) with Xenon lamp of 300 W. About 50mg sample was

dispersed in 20 ml 0.5 M Na_2SO_3. Prior to irradiation the reaction set up was purged with He (20 ml/min for 1 hr) to remove the air and then purged with high purity CO_2 (1bar, 5 ml/min) for 1 hr. During irradiation, 1 ml of gaseous product from the set-up was sampled and subsequent analysis was done by Gas Chromatography (Shimadzu Tracera GC-2010 Plus) with Barrier Ionization Detector (BID) and He carrier gas. Blank experiments were carried out in absence of CO_2 and light to confirm that these two factors are indispensable for photocatalytic CO_2 reduction reaction. For stability test, the selected photocatalyst was collected after each run, refreshed by washing with water and its performance was re-evaluated by the aforementioned procedure.

The selectivity of formed CO was deduced according to the following equation [50]

$$\% \text{ of CO selectivity} = \frac{2N_{CO}}{2N_{CO} + 2N_{H2}} \times 100$$

Here, N_{CO} and N_{H2} stand for the yield of reactively formed CO and H_2, respectively.

Apparent quantum yield (AQY) of the photocatalyst was calculated using the following equation[50]:

$$\text{AQY } \% = \frac{\text{The number of evolved CO molecules} \times 2}{\text{The number of incident photons}} \times 100$$

3. RESULTS AND DISCUSSION:

In the present study, the composite $C_3N_4/FeWO_4$ was synthesized by simple ultrasonic assisted (sonochemical) method followed by post-thermal treatment which is illustrated schematically in **Scheme 1.**Individually, C_3N_4 nanosheets and $FeWO_4$ nanoparticles were ultrasonicated to get exfoliated C_3N_4 nanosheets and uniformly dispersed $FeWO_4$nanoparticles. In the next step, the two solutions were mixed together and ultrasonicated again which allows the coupling between C_3N_4 and $FeWO_4$ through electrostatic interactions. The positively and negatively charged surfaces of C_3N_4 and $FeWO_4$,respectively,help them assemble into heterojunction configurations driven by the forces of electrostatic attraction as confirmed by Zeta potential data [19,34,50,51] presented in the supporting information Figure S1.Further, the attachment is enhanced by thermal treatment given to composite at 400°C for 2hrs.With the above-mentioned protocol 80 wt.%, 50 wt.% and 30 wt.% $C_3N_4/FeWO_4$ composites were prepared and evaluated for photocatalytic reduction of CO_2.

The crystal structures of C_3N_4,$FeWO_4$ and their composites were confirmed by XRD as given in **Figure 1**.The pristine C_3N_4 showed two characteristic peaks at 13.0° and 27.4° indexed respectively to (100) diffraction plane corresponding to in-plane packing motif of tri-s-triazine and (002) plane corresponding to interlayer stacking of aromatic rings.[18,50] For $FeWO_4$ all the peaks are well matched with (JCPDF-0712390) confirming Wolframite family with monoclinic crystal structure. Besides, no other phases were observed indicating the phase purity of samples. In all the cases of composites, characteristic peaks of C_3N_4 and $FeWO_4$ were observed indicating the co-existence of both the phases.

Neither any shift in the peaks nor any other impurity peaks were observed. Although, the characteristic peak of C_3N_4 in 30% composite is not clearly seen (though it can be clearly seen on the log scale as shown in the supporting information S2), but as the percentage of C_3N_4 is increased in the composite the peak of (002) plane can be seen distinctly especially in the case of 80% $C_3N_4/FeWO_4$.

FESEM and TEM were employed to investigate the morphology and the microstructure of the as-prepared samples. **Figure 2**a shows stacked curly 2D nanosheet like structure of C_3N_4, whereas Figure 2b displays cuboid like nanoparticles of $FeWO_4$ with particle size of ~ 40-50 nm. In the composite case (Figure 2c), stacked and compact nanosheet of C_3N_4 loaded with nano particles of $FeWO_4$ is seen. It can be seen from the image that particles are not only decorated on the sheet but are also present in between the stacked nanosheets of C_3N_4.In either case, it is clear that the $FeWO_4$ nanoparticles are firmly anchored onto the C_3N_4 nanosheets. Elemental Dispersive X-ray Spectroscopy (EDS) spectra (supporting information S3) and Elemental mapping (supporting information S4) of composite (80 wt. % $C_3N_4/FeWO_4$) clearly indicates that sample is composed of elements C, N, Fe, W and O and there is uniform distribution of $FeWO_4$ nanoparticles on the surface of C_3N_4 nanosheets.

The TEM image in Figure 2d also confirms the 2D nanosheet like morphology of C_3N_4. On the other hand, $FeWO_4$ shows cuboid like nanoparticles of size ~ 40 nm as presented in Figure 2e. In the composite, aggregates of $FeWO_4$ nanoparticles with increased size

of ~ 50-60 nm were seen to be embedded on ultrathin nanosheet of C_3N_4.The HRTEM images given in Figure 2 g and 3h denote the d-spacing of 0.325 nm and 0.377 nm corresponding to (002) plane of C_3N_4 and (110) plane of $FeWO_4$, respectively. Similarly, in the composite case, both the planes are seen indicating close proximity of the two components in the composite. No particles are seen to be separated or unanchored from nanosheet implying strong interaction between C_3N_4 and $FeWO_4$ which can form heterojunction structure instead of a simple physical mixture. Formation of such heterojunction between the two components can promotes favorable charge transfer of photogenerated charges at the interface junction.

Nitrogen absorption–desorption isotherms (Supporting information Figure S5) of C_3N_4, $FeWO_4$ and 80% $C_3N_4/FeWO_4$ samples show type IV adsorption-desorption isotherms characteristic with H3 hysteresis loop indicating slit like mesopores (2-50 nm) generated by aggregation of sheets like material or particles respectively, whereas in case of composite much more narrower slit like pores are generated. The results presented in Table S1 indicate lower surface area, pore volume and pore diameter of composite as compared to pristine C_3N_4 and $FeWO_4$. The decline in the different parameters of composite implies that nano particles of $FeWO_4$ are filling the original slit pores of C_3N_4 matrix making it much narrower, ultimately leading to the high degree of interfacial contact between C_3N_4 and $FeWO_4$.

The FTIR spectra of C_3N_4, $FeWO_4$ and (30 wt. %, 50 wt. % and 80 wt. %) $C_3N_4/FeWO_4$ are given in **Figure 3.**In pure C_3N_4, the peak at 1628 cm^{-1} corresponds to C-N stretching

vibration modes while the peaks at 1410,1323 and 1235 cm^{-1} belong to aromatic C-N stretching. The characteristic peak at 809 cm^{-1} is ascribed to the breathing modes of tris-triazine units.[18,50] In the IR spectrum of $FeWO_4$,the peaks at 500 cm^{-1} and 550 cm^{-1} are assigned to asymmetric vibrational mode of Fe-O whereas the peaks at 633 cm^{-1} and 700 cm^{-1} correspond to the stretching modes of W-O. The broad band at 844 cm^{-1} is the characteristic peak of asymmetric vibration of the bridge oxygen atom of Fe-O-W.[37,52] In the FTIR spectrum of composites, all the peaks of C_3N_4 and $FeWO_4$ are seen but major shift is seen in Fe-O and W-O vibrational modes. Similarly, in Fe-O-W mode red shift is seen with the increased introduction of C_3N_4 in the composite as given in enlarged inset figure of FTIR. Inversely, the characteristic vibrational modes of tris-s-triazine units in C_3N_4 also showed gradual red shift with increased introduction of $FeWO_4$ in the composite. Such kind of simultaneous shift in the characteristic peaks of C_3N_4 and $FeWO_4$ in composite photocatalyst implies strong interaction at the $C_3N_4/FeWO_4$ heterostructure interface.

To discover the surface chemical bonds of the photocatalyst, XPS data was recorded and are presented in **Figure 4.** In figure 4a, C1s spectra of pure C_3N_4 and 80 wt.% $C_3N_4/FeWO_4$ are compared. The peak centered at 284.6 eV corresponds to C-C bond, whereas peak at 288 eV corresponds to tertiary carbon C-N_3.[33,34,19] Both the peaks are present in pure C_3N_4 as well as in the composite without any shift. In the N1s spectrum (Figure 4b), three binding energies 398.9 eV (C=N-C),400.3 eV (C_3-N) and 401.5 eV (N-H) are attributed to pure C_3N_4which are shifted to lower binding energy in $C_3N_4/FeWO_4$

composite, indicating the change in the chemical environment of C_3N_4 after introduction of $FeWO_4$.[33,34,19] Similar fact was also observed in the O1s spectrum given in Figure 4c.Five deconvulated peaks in the case of O1s spectrum of $FeWO_4$ are seen corresponding to the lattice oxygen of Fe-O (529.8 eV), -OH bond (530.7 eV), metallic oxide of Fe-O (531.4 eV),W-O-W (532.4 eV) and water molecule (533.4 eV) adsorbed on the surface, respectively [40]The same five peaks are also present in the composite but with downward shift in binding energy. The shifts in the O1s and N1s contributions establish that C_3N_4 and $FeWO_4$ have formed a heterostructure and the composite is not a simple physical mixture. This is of immense significance for the transfer of photogenerated charges across the interface as discussed later. In the Fe 2p spectra of $FeWO_4$ and $C_3N_4/FeWO_4$ composite, two main peaks of $2p_{3/2}$ and $2p_{1/2}$ are seen without presence of any satellite peak which indicates that Fe exists in pure + 2 state. Similarly, in W 4f spectrum two symmetric peaks of $4f_{5/2}$ and $4f_{7/2}$ are seen indicating W + 6 oxidation state.[40]

To investigate and understand the opto-electronic properties of the prepared photocatalyst under study, UV-visible diffuse reflectance spectroscopy (UV-Vis DRS), photoluminescence (PL) and Mott-Schottky measurements were performed. From the DRS spectra given in **Figure 5**,it is clear that C_3N_4 has an absorption band edge at around 440 nm corresponding to band gap of 2.8 eV calculated from Tauc plot given in supporting information Figure S6 a, which is in agreement with previously reported values.[8,9,19]In contrast, $FeWO_4$ exhibits wide absorption range till 530 nm corresponding to a band gap

of 2.3 eV (Figure S6 b).Markedly, different from the absorption features of pristine C_3N_4 and $FeWO_4$, the composite 80 wt.% $C_3N_4/FeWO_4$ shows two distinct optical absorption edges ascribed to the intrinsic absorption edges of individual components. This implies combined optical absorption property of C_3N_4 and $FeWO_4$.

The photoluminescence (PL) analysis was performed to study the interfacial charge transfer and separation efficiency of photogenerted electrons and holes in $C_3N_4/FeWO_4$.The PL spectra given in Figure 6a display a broad PL emission peak centered at 455 nm for pristine C_3N_4 which is in line with the previous reports.[34,50] The peak is attributed to the band to band PL due to recombination of photo carriers in C_3N_4. In addition, strong PL quenching is possibly observed in case of $C_3N_4/FeWO_4$ composite suggesting the suppressed carrier recombination and improved charge separation, owing to the formation of $C_3N_4/FeWO_4$ heterostructure with strong interaction. Furthermore, charge transfer and separation efficiency were evaluated by transient photocurrent response given in Figure 6b.The strong photocurrent in the case of $C_3N_4/FeWO_4$ compared to pristine C_3N_4 reveals the higher separation rate of photocharges in the composite. Similarly, low charge transfer resistance in composite $C_3N_4/FeWO_4$ compared to pristine samples is observed by Electrochemical Impedance Spectra (EIS) given in supporting information S7. The reason lies in well-built interface of $C_3N_4/FeWO_4$ composite which is in good agreement with PL data as well as with the interpretation based on various aforementioned characterization techniques.

Further, Mott-Schottky (MS) analysis was done to investigate the fermi levels of the photocatalyst. The positive slopes of Mott- Schottky plots (Figure 6c and d) indicate n-type semiconducting feature of C_3N_4 and $FeWO_4$. Moreover, from the extrapolation of straight line to the x-intercept, calculated flat band potential (equivalent to conduction band) values for C_3N_4 and $FeWO_4$ are -1.35 V vs NHE and 0.42 V vs (NHE), respectively. The values indicate that CB of C_3N_4 is much more favorable for reduction reaction as compared to $FeWO_4$.The valence band values for C_3N_4 and $FeWO_4$ are 1.5 V and 2.8V vs NHE, respectively which were derived from UV-vis DRS spectra.

3.1 Photocatalytic Activity of $C_3N_4/FeWO_4$:

The photocatalytic CO_2 reduction performance of the pristine and composite photocatalysts was evaluated under solar light using Na_2SO_3 as a hole scavenger. The products were analyzed in regular interval of 1 hr as shown in Figure 7. CO ($CO_2 + 2H^+ + 2e^- \rightarrow CO + H_2O$) was found to be the main and direct product of photocatalytic CO_2 reduction. However, H_2 ($2H^+ + 2e^- \rightarrow H_2$) was also detected due to water splitting reaction, whereas holes are consumed by Na_2SO_3 ($NaSO_3 + 2OH^- + 2h^+ \rightarrow Na_2SO_4 + H_2O$).The control experiments (supporting information figure S8) in the absence of photocatalyst or light or CO_2 were also performed, confirming that the obtained CO is solely originating from CO_2 photoreduction and also illustrates that light, CO_2 and photocatalyst are essential for the photocatalytic CO_2 reduction.

Very interestingly, $C_3N_4/FeWO_4$ composites showed excellent performances for photocatalytic CO_2 reduction under solar light irradiation as shown in Figure 7a. After 5hrs of irradiation, optimum photocatalytic activity over 80 wt. % $C_3N_4/FeWO_4$ was 30.6 μmol/g, which is almost 6-folds and 15-folds higher as compared to pristine C_3N_4 (6.02 μmol/g) and $FeWO_4$ (1.94 μmol/g) samples, respectively. The optimum CO production rate of 80 wt. % $C_3N_4/FeWO_4$ is also relatively higher than the other composites: 30% $C_3N_4/FeWO_4$ (18.9 μmol/g) and 50% $C_3N_4/FeWO_4$ (22.9 μmol/g). The low performance of C_3N_4 and $FeWO_4$ can be attributed to the electron-hole recombination prevailing in the system. Additionally, $FeWO_4$ possesses unfavorable energy levels for CO_2 reduction as seen from the MS plot (Figure 6d). Although, during photocatalytic CO_2 reduction, the undesired H_2 evolution from water splitting is also observed (Figure 7b), but the CO selectivity is greater than 90% over H_2 evolution. Notably, the selectivity of CO for 80 wt. % $C_3N_4/FeWO_4$ is almost 100% over hydrocarbons as no CH_4 or any other higher hydrocarbons were seen to evolve. Furthermore, the measured apparent quantum efficiency (AQE) for the 80 wt.% $C_3N_4/FeWO_4$ composite using 420 nm band pass filter is significant (~ 0.3%), and higher than the prior reported literature.[53,54,55]

It is well-known that the catalyst reusability is always a critical issue for long run performance of CO_2 reduction in practical applications. In order to investigate the stability of the $C_3N_4/FeWO_4$ composite, three successive cyclic experimental runs were performed under the same experimental conditions. Each run was conducted after evacuation and purging of fresh CO_2 in the set up. As shown in Figure 8, the photocatalytic CO evolution

of composite is nearly constant even after 3 successive experimental runs of total 18 hrs of illumination. A slight decrease after 3rd cycle, retaining almost 97% original activity, is observed which may be due to inevitable loss of the catalyst during cyclic run. The reusability results are a direct evidence of firm attachment of $FeWO_4$ to C_3N_4 nanosheets, also indicating a strongly built-in heterojunction between them to produce a constant outcome throughout the long run.

3.2 Photocatalytic mechanism:

In order to understand the mechanism for enhanced photocatalytic activity for CO_2 reduction of the $C_3N_4/FeWO_4$ composites, band line-ups were obtained w.r.t. to CO_2 reduction potential, with the values derived from UV-Vis DRS and Mott Schottky plots. The derived energy level diagram given in Figure 9 clearly indicates that the conduction band (CB) edge of C_3N_4 is just above the reduction potential of CO_2 (-0.51V vs NHE) [8,9] whereas that of $FeWO_4$ is below it. Thus, C_3N_4 has much more favorable energy levels compared to $FeWO_4$ individually but interestingly as a composite they exhibit enhanced photocatalytic activity.

Considering the band structures of C_3N_4 and $FeWO_4$ two possible charge transfers are possible: Type II heterojunction and direct Z-scheme. According to conventional type II heterojunction which is band to band charge transfer, the photogenerted electrons from the CB of C_3N_4 must be transferred to CB of $FeWO_4$ where CO_2 reduction is expected to occur, on other hand, holes are transferred from VB of C_3N_4 to VB of $FeWO_4$. However,

our catalytic activity and band-structure results clearly show this to be unlikely in the present heterostructure system due to unfavorable energy levels of $FeWO_4$ for CO_2 reduction to CO. Therefore, due to band-structure matching, Z-scheme is the feasible mechanism in the present system. In the Z-scheme $C_3N_4/FeWO_4$ composite system, the C_3N_4 and $FeWO_4$ photocatalysts are in contact with band matching in such a way that electrons from the CB of $FeWO_4$ will combine with the holes from the VB of C_3N_4 after photo excitation, leaving electron in C_3N_4, where CO_2 reduction to CO take place due to appropriate band potential for CO formation, and hole in $FeWO_4$, i.e electrons and hole are in spatially separated in different locations. This kind of spatially separated photocatalytic systems has great advantage as efficient charge separation can be achieved and thereby high performance is realized for photocatalytic reactions.

As seen from a Figure 9 $FeWO_4$ has relatively negative conduction potential (0.42 V vs NHE) w.r.t. to C_3N_4 valence band potential (1.5 V vs NHE) which effectively favors the Z-scheme mechanism. As a result, electrons in CB of C_3N_4 with high reducibility are greatly preserved (which would otherwise combine with its own holes from VB) whereas holes in the VB of $FeWO_4$ with their high oxidizibility are preserved. Consequently, more photogenerated electrons are available to perform photocatalytic reduction of CO_2. Ultimately, CO yield and selectivity both are enhanced in the $C_3N_4/FeWO_4$ composite as compared to its pure counterparts. Notably, despite the unfavorable energy levels of $FeWO_4$ for the CO_2 reduction, only 20% addition of $FeWO_4$ in the composite (80 wt. % $C_3N_4/FeWO_4$) has shown an immense enhancement in photocatalytic CO_2 reduction as

compared to 100% C_3N_4, which justifies the possible direct scheme mechanism. To confirm the role of $FeWO_4$ and Z-scheme mechanism in the present system, we studied the hydroxyl radical formation using terephthalic acid as a probe molecule in PL analysis. It is well-know that the terephthalic acid readily combines with ·OH radical and forms 2-hydroxyterephthalic acid which shows PL emission peak around 425 nm. Comparison of PL intensity for all the samples against irradiation time was monitored and given in Figure 10 b. For $FeWO_4$ (Supporting information figure S 9) and composite $C_3N_4/FeWO_4$ sample (Figure 10 a) gradual increase in PL intensity was observed as compared to C_3N_4, indicating the formation of ·OH radical on their surfaces upon illumination except for C_3N_4.Considering the relative band edge positions of C_3N_4 and $FeWO_4$ along with standard redox potentials of $OH^-/{}^{\cdot}OH$ (2.5V vs NHE) and $O_2/{}^{\cdot}O_2^-$ (-0.3V vs NHE) [33,56] given in Figure 9,only photogenerated holes in the VB of pristine $FeWO_4$ and $FeWO_4$ present in the composite $C_3N_4/FeWO_4$ can produce ·OH radical whereas photogenerated electrons in C_3N_4 are able to produce only supraoxide radical anion·O_2^-.If the obtained composite $C_3N_4/FeWO_4$ would have followed conventional heterojunction mechanism then neither ·OH radical nor superoxide radical anion ·O_2 would be produced, thus resulting in subsequent absence of the PL signal. However, strong PL signal in the composite was seen to increase linearly with time and has intensity greater than that for pristine $FeWO_4$ as shown in Figure 10 b. Thus, ·OH radicals were indeed produced in the case of the composite which confirms the direct Z-scheme mechanism in $C_3N_4/FeWO_4$ instead of conventional heterojunction type. Consequently, the prevailing recombination

in C_3N_4 is highly suppressed (evident from PL and on-off transient) as the holes from VB of C_3N_4 are very well quenched by electrons from CB of $FeWO_4$ under Z scheme mechanism, preserving the photogenerated electrons in C_3N_4 for photocatalytic CO_2 reduction. Thus, coupling of $FeWO_4$ with C_3N_4 under Z scheme mechanism has not only induced efficient charge separation in C_3N_4 but also restored its reducing capability resulting in almost 6-fold enhancement in photocatalytic performance along with high CO selectivity.

4. CONCLUSIONS:

In summary, a direct Z-scheme $C_3N_4/FeWO_4$ photocatalytic system was constructed by simple sonochemical method followed by post annealing treatment which assembled the two components in the composite through electrostatic attraction and through thermal attachment. The resultant composite exhibited excellent photocatalytic performance and selectivity for CO_2 reduction. The optimum $C_3N_4/FeWO_4$ showed highest CO production rate of 6 μmol/g/hr which is almost 6 times and 15 times higher than pure-C_3N_4 and $FeWO_4$ phases, respectively. Moreover, it showed almost ~ 91% CO selectivity with no CH_4 or any other higher hydrocarbon evolution. The overall performance of new photocatalytic system is ascribed to the direct Z scheme mechanism with appropriate band matching of $FeWO_4$ with respect to C_3N_4 band edges. The novel coupling under Z-scheme mechanism of hybrid photocatalyst not only favors superior charge separation of electron-hole pair in C_3N_4 but also restores the reducibility of C_3N_4 for CO_2

photoreduction. Importantly, the Z scheme photocatalyst was photostable even after successive experimental runs, without any obvious change in the activity. The present work provides significant insights for constructing a stable functional composite via Z-scheme for selective photocatalytic reduction of CO_2.

ASSOCIATED CONTENT

Supporting Information

Zeta Potential measurement, EDS, Elemental mapping, BET measurements, Tauc plot, EIS spectra, Photocatalytic control experiment, Time dependent PL of $FeWO_4$ in terephthalic acid.

AUTHOR INFORMATION

Corresponding Author

Email: satishogale@gmail.com, S.Kumar@bath.ac.uk

ACKNOWLEDGEMENTS

We thank DST Nanomission (Thematic Unit SR/NM/TP-13/2016), Govt. of India for research grant. SK also thanks the Engineering and Physical Sciences Research Council (EPSRC) (EP/R026041/1) for financial support.

5. REFERENCES

(1) Van der Hoeven, M. CO_2 Emisssions From Fuel Combustion Highlights. *Int. Energy Agency* **2014**, 1–134.

(2) Canadell, J. G.; Klepper, G.; Raupach, M. R.; Marland, G.; Ciais, P.; Que, C. Le; Field, C. B. Global and Regional Drivers of Accelerating CO_2 Emissions ´ Re. *PNAS* **2007**, *104* (24), 10288–10293.

(3) Mikkelsen, M.; Jørgensen, M.; Krebs, F. C. The Teraton Challenge . A Review of Fixation and Transformation of Carbon Dioxide. *Energy Environ. Sci.* **2010**, *3* (3), 43–81.

(4) Li, K.; Peng, B.; Peng, T. Recent Advances in Heterogeneous Photocatalytic CO_2 Conversion to Solar Fuels. *ACS Catal.* **2016**, No. 6, 7485–7527.

(5) Lingampalli, S. R.; Ayyub, M. M.; Rao, C. N. R. Recent Progress in the Photocatalytic Reduction of Carbon Dioxide. *ACS Omega* **2017**, *2*, 2740–2748.

(6) Chang, X.; Wang, T.; Gong, J. CO_2 Photo-Reduction: Insights into CO_2 Activation and Reaction on Surfaces of Photocatalysts. *Energy Environ. Sci.* **2016**, *9* (7), 2177–2196.

(7) Xie,S; Zhang,Q;Liu,G;Wang,Y.Photocatalytic and Photoelectrocatalyticreduction of CO_2 using heterogeneous catalysts with controlled nanostructures *Chem. Commun.***2016**, *52*, 35–59.

(8) Zhu, J.; Xiao, P.; Li, H.; Carabineiro, A. C. Graphitic Carbon Nitride : Synthesis , Properties, and Applications in Catalysis. *ACS Appl. Mater. Interfaces* **2014**, *6* (6), 16449–16465.

(9) Ye, S.; Wang, R.; Wu, M.; Yuan, Y. A Review on G-C_3N_4 for Photocatalytic Water Splitting and CO_2 Reduction. *Appl. Surf. Sci.* **2015**, *358*, 15–27.

(10) Cao, S.; Low, J.; Yu, J.; Jaroniec, M. Polymeric Photocatalysts Based on Graphitic Carbon Nitride. *Adv. Mater.* **2015**, *27*, 2150-2176.

(11) Liu, J.; Huang, J.; Zhou, H.; Antonietti, M. Uniform Graphitic Carbon Nitride Nanorod for Efficient Photocatalytic Hydrogen Evolution and Sustained Photoenzymatic Catalysis. *ACS*

Appl. Mater. Interfaces **2014**, *6*, 8434–8440.

(12) Zheng, D.; Cao, X.; Wang, X. Precise Formation of a Hollow Carbon Nitride Structure with a Janus Surface To Promote Water Splitting by Photoredox Catalysis. *Angew. Chemie - Int. Ed.* **2016**, *55*, 11512–11516.

(13) Ran, J.; Ma, T. Y.; Gao, G.; Du, X.; Qiao, S. Z. Porous P-Doped Graphitic Carbon Nitride Nanosheets for Synergistically Enhanced Visible-Light Photocatalytic H_2 Production. *Energy Environ. Sci.* **2015**, *8*, 3708–3717.

(14) Kong, L.; Dong, Y.; Jiang, P.; Wang, G.; Zhang, H.; Zhao, N. Light-Assisted Rapid Preparation of a Ni/g-C_3N_4 Magnetic Composite for Robust Photocatalytic H_2 Evolution from Water. *J. Mater. Chem. A* **2016**, *4*, 9998–10007.

(15) Gao, G.; Jiao, Y.; Waclawik, E. R.; Du, A. Single Atom (Pd / Pt) Supported on Graphitic Carbon Nitride as an Efficient Photocatalyst for Visible-Light Reduction of Carbon Dioxide. *JACS* **2016**, *138*, 6292–6297.

(16) Li, H.; Gan, S.; Wang, H.; Han, D.; Niu, L. Intercorrelated Superhybrid of AgBr Supported on Graphitic-C_3N_4 -Decorated Nitrogen-Doped Graphene: High Engineering Photocatalytic Activities for Water Purification and CO_2 Reduction. *Adv. Mater.* **2015**, *27*, 6906–6913.

(17) Cometto, C.; Kuriki, R.; Chen, L.; Maeda, K.; Lau, T.; Ishitani, O.; Robert, M. A Carbon Nitride/Fe Quaterpyridine Catalytic System for Photostimulated CO_2 to CO Conversion with Visible Light. *JACS* **2018**, *140*, 7437–7440.

(18) Yu, W.; Peng, T. Selective CO_2 Reduction to CH_3OH via Facile Coupling of ZnO : A Direct Z-Scheme Mechanism. *J. Mater. Chem. A* **2015**, *3*, 19936–19947.

(19) Di, T.; Zhu, B.; Cheng, B.; Yu, J.; Xu, J. A Direct Z-Scheme g-C_3N_4 /SnS_2 Photocatalyst with Superior Visible-Light CO_2 Reduction Performance. *J. Catal.* **2017**, *352*, 532–541.

(20) Nie, N.; Zhang, L.; Fu, J.; Cheng, B.; Yu, J. Self-Assembled Hierarchical Direct Z-Scheme g-C_3N_4/ZnO Microspheres with Enhanced Photocatalytic CO_2 Reduction Performance. *Appl. Surf. Sci.* **2018**, *441*, 12–22.

(21) Reli, M.; Huo, P.; Marcel, S.; Ambrozova, N.; Troppova, I.; Matejova, L.; Lang, J.; Svoboda, L.; Kustrowski, P.; Ritz, M.; Praus, P; Koci, K. Novel TiO_2/C_3N_4 Photocatalysts for Photocatalytic Reduction of CO_2 and for Photocatalytic Decomposition of N_2O. *J. Phys. Chem. A* **2016**, *120*, 8564–8573.

(22) Dhakshinamoorthy, A.; Navalon, S.; Garcia, H. Photocatalytic CO_2 Reduction by TiO_2 and

Related Titanium Containing Solids. *Energy Environ. Sci.* **2012**, *5*, 9217–9233.

(23) Cao, S.; Liu, X.; Yuan, Y.; Zhang, Z.; Liao, Y. Solar-to-Fuels Conversion over In_2O_3/g-C_3N_4 Hybrid Photocatalysts. *Appl. Catal. B Environ.* **2014**, *147*, 940–946.

(24) Shi, H.; Chen, G.; Zhang, C.; Zou, Z. Polymeric G-C_3N_4 Coupled with $NaNbO_3$ Nanowires toward Enhanced Photocatalytic Reduction of CO_2 into Renewable Fuel. *ACS Appl. Mater. Interfaces* **2014**, *4* (4), 3637–3643.

(25) He, Y.; Zhang, L.; Teng, B.; Fan, M. New Application of Z-Scheme Ag_3PO_4/g-C_3N_4 Composite in Converting CO_2 to Fuel. *Environ. Sci. Technol.* **2015**, *49*, 649–656.

(26) Low, J.; Jiang, C.; Cheng, B.; Wageh, S.; , Ahmed AAl-ghamdi, Y. J. A Review of Direct Z-Scheme Photocatalysts. *Small* **2017**, *1*, 1700080.

(27) Li, H.; Tu, W.; Zhou, Y.; Zou, Z. Z-Scheme Photocatalytic Systems for Promoting Photocatalytic Performance : Recent Progress and Future Challenges. *Adv. Sci.* **2016**, *1500389*, 1–12.

(28) Yu, J.; Wang, S.; Low, J.; Xiao, W. Enhanced Photocatalytic Performance of Direct Z-Scheme g-C_3N_4-TiO_2 photocatalysts for the Decomposition of Formaldehyde in Air. *Phys. Chem. Chem. Phys.* **2013**, *15* (39), 16883–16890.

(29) Liu, J.; Cheng, B.; Yu, J. A New Understanding of the Photocatalytic Mechanism of the Direct Z-Scheme g-C_3N_4/TiO_2 heterostructure. *Phys. Chem. Chem. Phys.* **2016**, *18* (45), 31175–31183.

(30) Yu, W.; Chen, J.; Shang, T.; Chen, L.; Gu, L.; Peng, T. Direct Z-Scheme g-C_3N_4/WO_3 photocatalyst with Atomically Defined Junction for H_2 production. *Appl. Catal. B Environ.* **2017**, *219*, 693–704.

(31) Meng, A.; Zhu, B.; Zhong, B.; Zhang, L.; Cheng, B. Direct Z-Scheme TiO_2/CdS Hierarchical Photocatalyst for Enhanced Photocatalytic H_2-Production Activity. *Appl. Surf. Sci.* **2017**, *422*, 518–527.

(32) Yang, Y.; Wang, S.; Li, Y.; Wang, J.; Wang, L. Strategies for Efficient Solar Water Splitting Using Carbon Nitride. *Chem. Asian J.* **2017**, *12* (12), 1421–1434.

(33) Xia, P.; Zhu, B.; Cheng, B.; Yu, J.; Xu, J. 2D/2D g-C_3N_4/MnO_2 Nanocomposite as a Direct Z-Scheme Photocatalyst for Enhanced Photocatalytic Activity. *ACS Sustain. Chem. Eng.* **2018**, *6*, 965–973.

(34) Xu, Q.; Zhu, B.; Jiang, C.; Cheng, B.; Yu, J. Constructing 2D/2D Fe_2O_3/g-C_3N_4 Direct Z-

Scheme Photocatalysts with Enhanced H_2 Generation Performance.*Solar RRL* **2018**,*2*, 1800006.

(35) Hu, L.; He, H.; Xia, D.; Huang, Y.; Xu, J.; Li, H.; He, C.; Yang, W.; Shu, D.; Wong, P. K. Highly Efficient Performance and Conversion Pathway of Photocatalytic CH_3SH Oxidation on Self-Stabilized Indirect Z-Scheme g-C_3N_4/I_3-BiOI. *ACS Appl. Mater. Interfaces* **2018**, *10* (22), 18693–18708.

(36) Wang, J.; Yao, H.; Fan, Z.; Zhang, L.; Wang, J.; Zang, S.; Li, Z. Indirect Z-Scheme BiOI / g-C_3N_4 Photocatalysts with Enhanced Photoreduction CO_2 Activity under Visible Light Irradiation. *ACS Appl. Mater. Interfaces* **2016**, *8*, 3765–3775.

(37) Buvaneswari, K.; Karthiga, R.; Kavitha, B.; Rajarajan, M.; Suganthi, A. Applied Surface Science Effect of $FeWO_4$ Doping on the Photocatalytic Activity of ZnO under Visible Light Irradiation. *Appl. Surf. Sci.* **2015**, *356*, 333–340.

(38) Gao, Q.; Liu, Z. Progress in Natural Science : Materials International $FeWO_4$ Nanorods with Excellent UV – Visible Light Photocatalysis. *Prog. Nat. Sci. Mater. Int.* **2017**, *27* , 556–560.

(39) Ma,Y; Guo,Y; Jiang,H; Qu,D; Liu,J; Kang,W; Yi,Y; Zhang,W; Shi,J; Han, Z; Preparation of Network-like ZnO–$FeWO_4$ Mesoporous Heterojunctions with Tunable Bandgaps and their Enhanced Visible Light Photocatalytic Performance. *New J. Chem.***2015**,*39* ,5612-5620.

(40) Jaffer, M. M.; Shenoy, U. S.; Bhat, D. K. Enhanced Photocatalytic Performance of N-Doped RGO-$FeWO_4$/Fe_3O_4 Ternary Nanocomposite in Environmental Applications. *Mater. Today Chem.* **2017**, *4*, 133–141.

(41) Tanaka, K.; Miyajima, T.; Shirai, N.; Zhuang, Q.; Nakata, R.; Tanakasal, K.; Miyajima, T.; Shirai, N.; Zhuang, Q.; Nakata, R. Laser Photochemical Ablation of $CdWO_4$ Studied with the Time of flight Mass Spectrometric Technique. *J.Appl. Phys.* **1998**, *77* (1995), 6581–6587.

(42) Zhang, Q. N. Temperature Dependence of the Polarized Raman Spectra of $ZnWO_4$ Single Crystals. *Phys. Rev. B* **1992**, *45* (18), 356–362.

(43) Qu, W.; Wlodarski, W. Comparative Study on Micromorphology and Humidity Sensitive Properties of Thin-Film and Thick-Film Humidity Sensors Based on Semiconducting MnWO4. *Sensors and Actuators* **2000**, *64* (64), 76–82.

(44) García-pérez, U. M.; Cruz, A. M.; Peral, J. Electrochimica Acta Transition Metal Tungstates Synthesized by Co-Precipitation Method : Basic Photocatalytic Properties. *Electrochim. Acta* **2012**, *81*, 227–232.

(45) Alshehri, S. M.; Ahmed, J.; Alzahrani, A. M.; Ahamad, T. Photocatalytic Properties of $NiWO_4$ Nanobricks. *New J. Chem.* **2017**, *41*, 8178–8186.

(46) Ye, D.; Li, D.; Zhang, W.; Sun, M.; Hu, Y.; Zhang, Y.; Fu, X. A New Photocatalyst $CdWO_4$ Prepared with a Hydrothermal Method. *J. Phys. Chem. C* **2008**, *112*, 17351–17356.

(47) Tressler, C. M.; Stonehouse, P.; Kyler, K. S. Calcium Tungstate : A Convenient Recoverable Catalyst for Hydrogen Peroxide Oxidation. *Green Chem.* **2016**, No.18, 4875–4878.

(48) He, G.; Chen, M.; Liu, Y.; Li, X.; Liu, Y.; Xu, Y. Applied Surface Science Hydrothermal Synthesis of $FeWO_4$ Graphene Composites and Their Photocatalytic Activities under Visible Light. *Appl. Surf. Sci.* **2015**, *351*, 474–479.

(49) Ma, J.; Tan, X.; Jiang, F.; Yu, T. Graphitic C_3N_4 Nanosheet-Sensitized Brookite TiO_2 to Achieve Photocatalytic Hydrogen Evolution under Visible Light. *Catal. Sci. Technol.* **2017**, No. 7, 3275–3282.

(50) Tonda, S.; Kumar, S.; Bhardwaj, M.; Yadav, P.; Ogale, S. G-CN/NiAl-LDH 2D/2D Hybrid Heterojunction for High- Performance Photocatalytic Reduction of CO into Renewable Fuels.*ACS Appl. Mater. Interfaces* **2017**, *10*, 2667–2678.

(51) Shanker, G. S.; Bhosale, R.; Ogale, S.; Nag, A. 2D Nanocomposite of G-C_3N_4 and TiN Embedded N-Doped Graphene for Photoelectrochemical Reduction of Water Using Sunlight.*Adv.Mater. Interface* **2018**,*1*, 1801488.

(52) Kovács, T. N.; Pokol, G.; Gáber, F.; Nagy, D.; Igricz, T.; Endre, I.; Fogarassy, Z.; Balázsi, K.; Szilágyi, I. M. Preparation of Iron Tungstate ($FeWO_4$) Nanosheets by Hydrothermal Method. *Mater. Research Bull.* **2017**, *95*, 563–569.

(53) An, X.; Li, K.; Tang, J. Cu_2O/Reduced Graphene Oxide Composites for the Photocatalytic Conversion of CO_2. *ChemSusChem* **2014**, *7*, 1086–1093.

(54) Kuehnel, M. F.; Orchard, K. L.; Dalle, K. E.; Reisner, E. Selective Photocatalytic CO_2 Reduction in Water through Anchoring of a Molecular Ni Catalyst on CdS Nanocrystals. *JACS* **2017**, *139*, 7217–7223.

(55) Article, E.; Zhang, G.; Lan, Z.; Lin, L.; Lin, S.; Wang, X. Overall Water Splitting by Pt/g-

C_3N_4 Photocatalysts Without without Using Sacrificial Agents. *Chem. Sci.* **2016**, *7*, 3062–3066.

(56) Meng, S.; Ning, X.; Zhang, T.; Chen, S.; Fu, X. What Is the Transfer Mechanism of Photogenerated Carriers for the Nanocomposite. *Phys. Chem. Chem. Phys.* **2015**, *17*, 11577–11585.

6. FIGURE CAPTIONS

Scheme1.Schematic illustration of synthesis process of hybrid photocatalyst $C_3N_4/FeWO_4$

Figure 1. XRD pattern of C_3N_4, $FeWO_4$ and different composites of $C_3N_4/FeWO_4$

Figure 2. (a), (b) and (c) FESEM images, (d), (e) and (f) TEM images and (g), (h) and (i) HRTEM images of C_3N_4, $FeWO_4$ and $C_3N_4/FeWO_4$, respectively.

Figure 3. FTIR spectra of C_3N_4, $FeWO_4$ and different composites of $C_3N_4/FeWO_4$.Inset enlarge FTIR shows the characteristics peaks of C_3N_4 and $FeWO_4$ and $C_3N_4/FeWO_4$, respectively, in the 750 cm^{-1} to 890 cm^{-1} region.

Figure 4.XPS spectrum of a) C 1s, b) N 1s, c) O 1s,d) Fe 2p and e) W 4f of C_3N_4, $FeWO_4$ and $C_3N_4/FeWO_4$.

Figure 5. DRS spectra of C_3N_4, $FeWO_4$ and $C_3N_4/FeWO_4$.

Figure 6. a) Photoluminous spectra b) On-off transient of C_3N_4 and $C_3N_4/FeWO_4$.Mott-Schottky plots of c) C_3N_4 and d) $FeWO_4$.

Figure 7.Time dependent a) CO and b) H_2 over the synthesized sample (Conditions: 50 mg photocatalyst and 300 W Xenon lamp with UV cut –off filter.

Figure 8. Stability profile of $C_3N_4/FeWO_4$.

Figure 9. Schematic illustration of photocatalytic mechanism in $C_3N_4/FeWO_4$.

Figure 10.a) PL spectral changes observed during illumination of the 80% $C_3N_4/FeWO_4$ sample in the presence of $5 * 10^{-4}$ M terephthalic acid in $2 * 10^{-3}$ M NaOH solution. b) Comparison of PL peak intensity around 425 nm for the C_3N_4, $FeWO_4$ and 80% $C_3N_4/FeWO_4$

7. FIGURES

Scheme 1

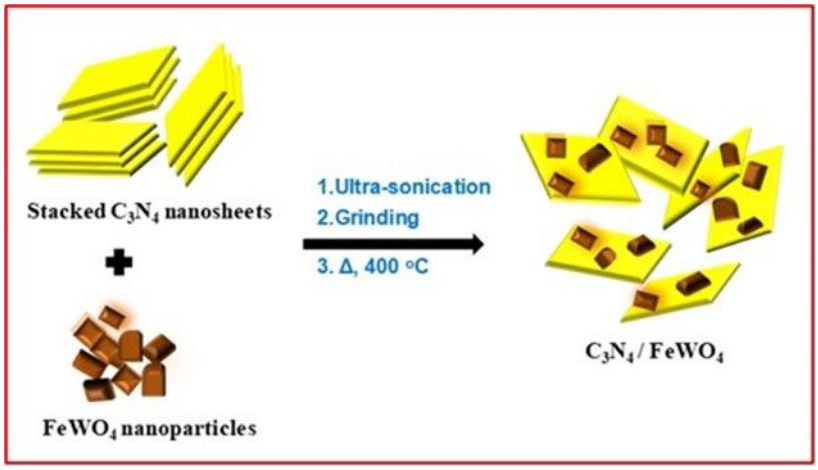
Stacked C_3N_4 nanosheets
$FeWO_4$ nanoparticles
1.Ultra-sonication
2.Grinding
3. Δ, 400 °C
C_3N_4 / $FeWO_4$

Figure 1

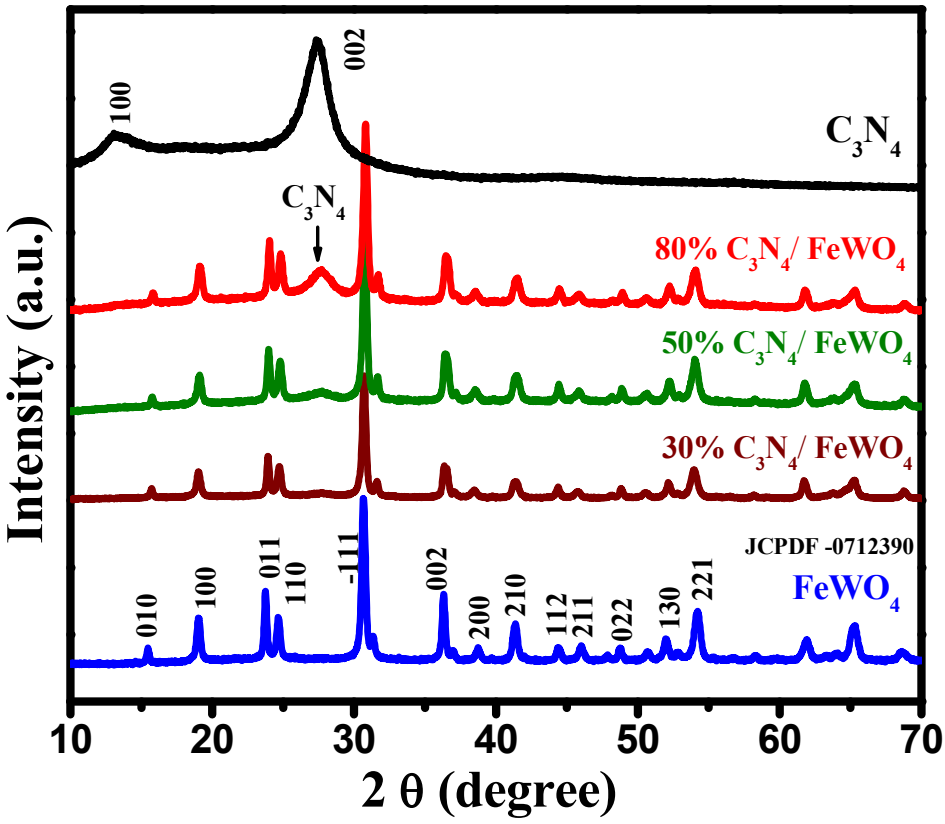
Intensity (a.u.)
2 θ (degree)
10
20
30
40
50
60
70
100
002
C3N4
C3N4
80% C3N4/ FeWO4
50% C3N4/ FeWO4
30% C3N4/ FeWO4
JCPDF -0712390
FeWO4
010
100
011
110
-111
002
200
210
112
211
022
130
221

Figure 2

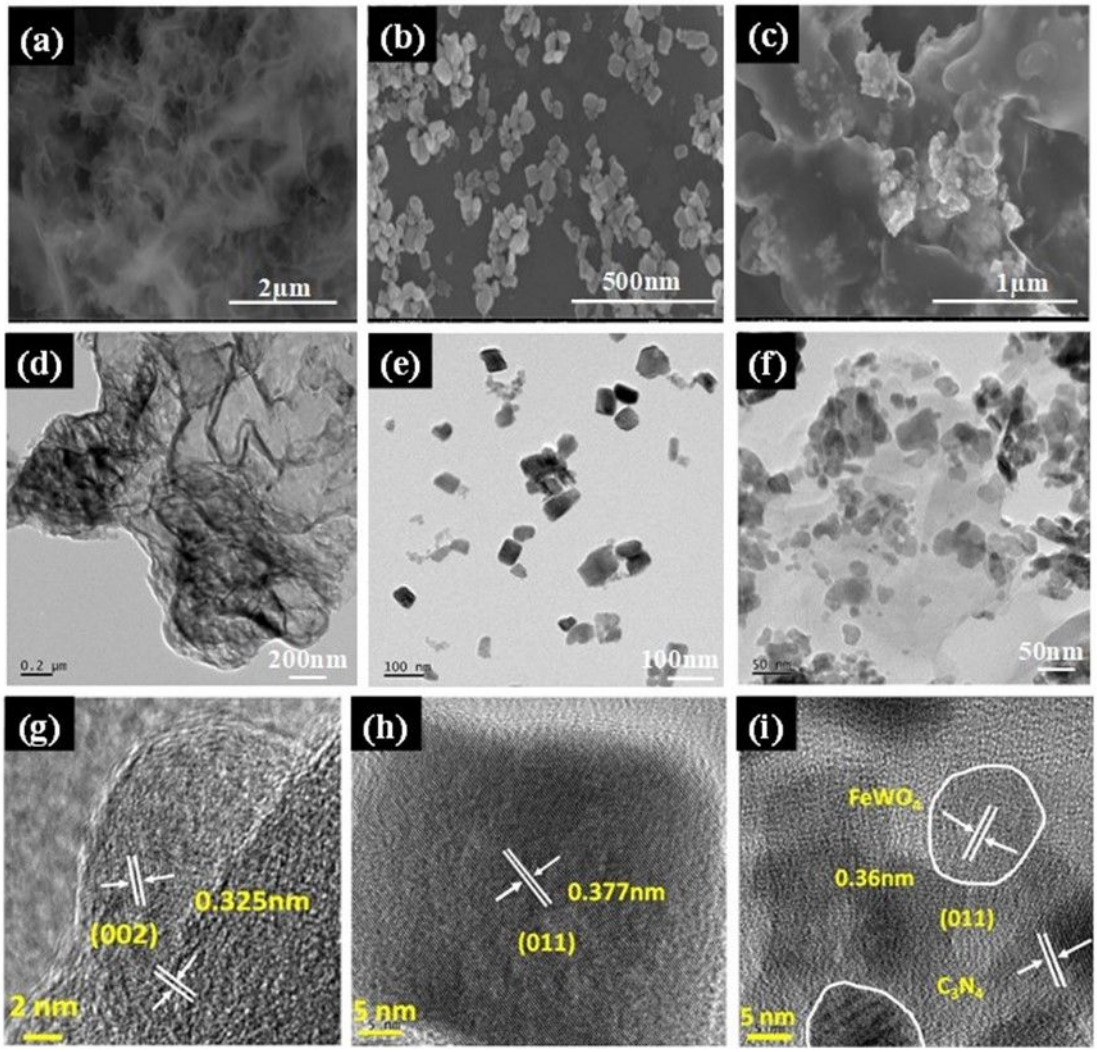
(a)
2μm
(b)
500nm
(c)
1μm
(d)
200nm
(e)
100nm
(f)
50nm
(g)
0.325nm
(002)
2 nm
(h)
0.377nm
(011)
5 nm
(i)
FeWO4
0.36nm
(011)
C3N4
5 nm

Figure 3

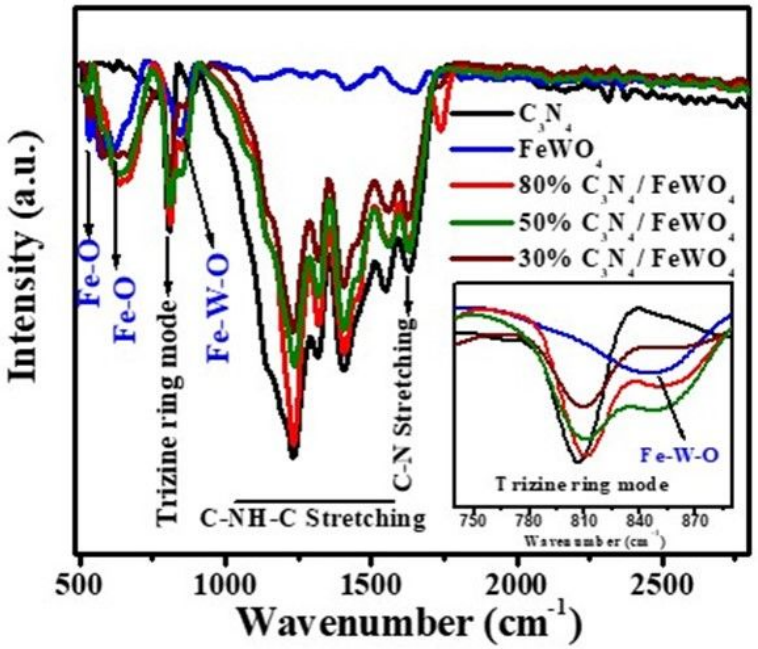
Intensity (a.u.)
Wavenumber (cm-1)
500
1000
1500
2000
2500
Fe-O
Fe-O
Trizine ring mode
Fe-W-O
C-NH-C Stretching
C-N Stretching
C3N4
FeWO4
80% C3N4 / FeWO4
50% C3N4 / FeWO4
30% C3N4 / FeWO4
Fe-W-O
Trizine ring mode
750
780
810
840
870
Wavenumber (cm-1)

Figure 4

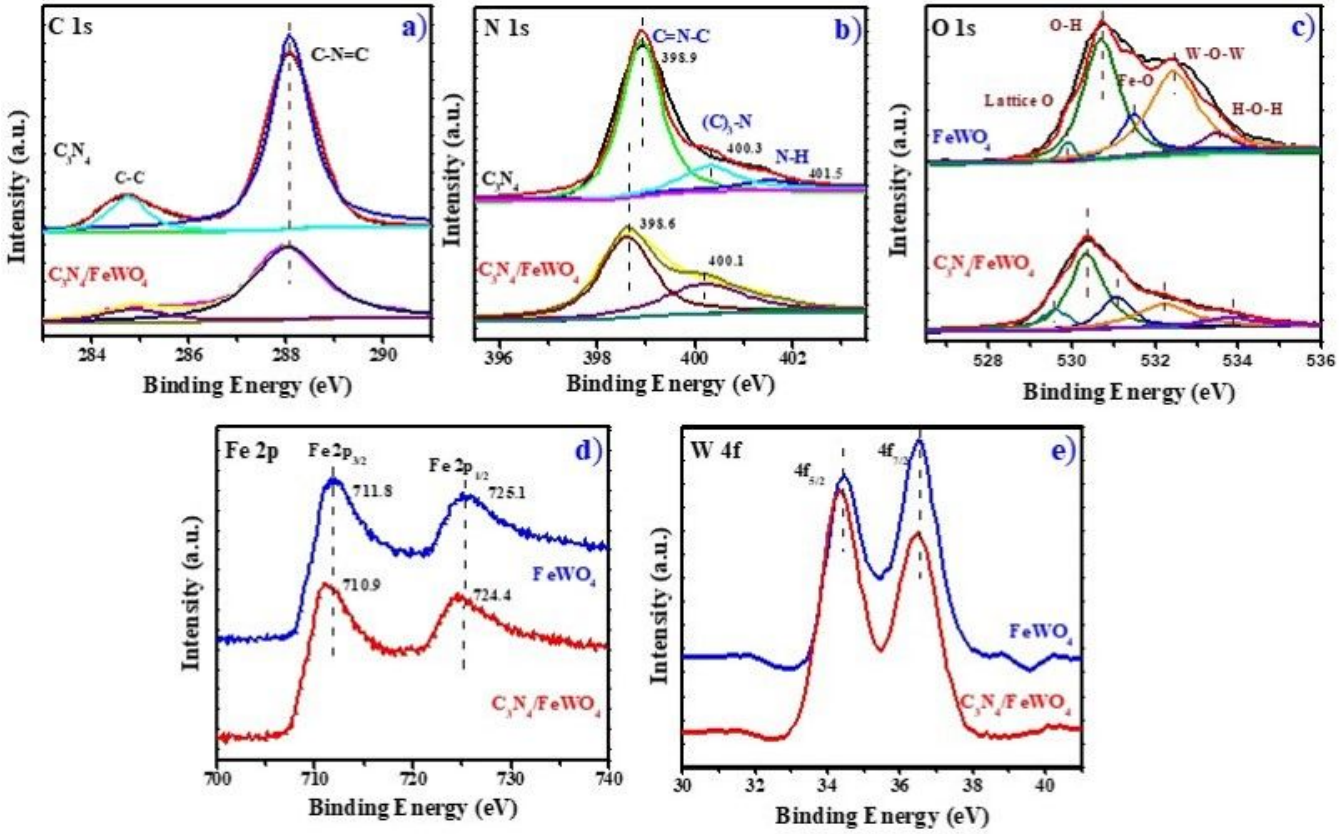
C 1s
a)
C-N=C
C-C
C_3N_4
C_3N_4/FeWO$_4$
Intensity (a.u.)
284
286
288
290
Binding Energy (eV)
N 1s
b)
C=N-C
398.9
$(C)_3$-N
400.3
N-H
401.5
C_3N_4
398.6
400.1
C_3N_4/FeWO$_4$
Intensity (a.u.)
396
398
400
402
Binding Energy (eV)
O 1s
c)
O-H
W-O-W
Fe-O
Lattice O
H-O-H
FeWO$_4$
C_3N_4/FeWO$_4$
Intensity (a.u.)
528
530
532
534
536
Binding Energy (eV)
Fe 2p
d)
Fe2p$_{3/2}$
Fe 2p$_{1/2}$
711.8
725.1
710.9
724.4
FeWO$_4$
C_3N_4/FeWO$_4$
Intensity (a.u.)
700
710
720
730
740
Binding Energy (eV)
W 4f
e)
4f$_{5/2}$
4f$_{7/2}$
FeWO$_4$
C_3N_4/FeWO$_4$
Intensity (a.u.)
30
32
34
36
38
40
Binding Energy (eV)

Figure 5

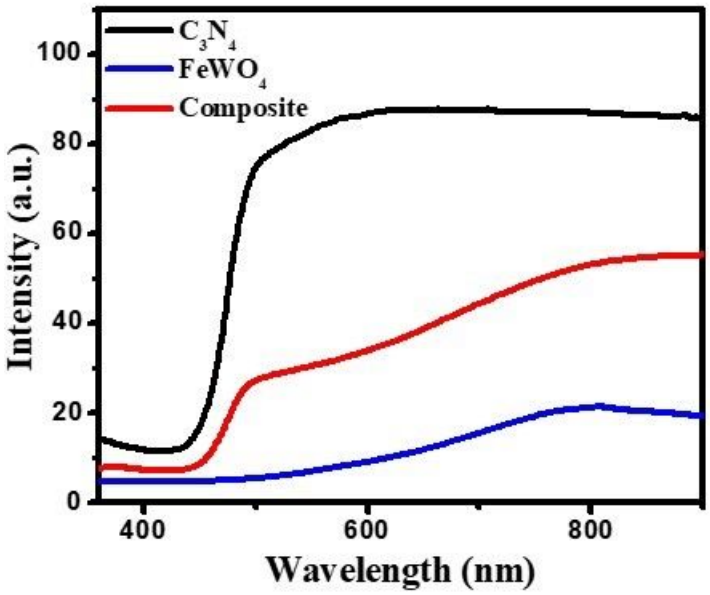
C3N4
FeWO4
Composite
Intensity (a.u.)
Wavelength (nm)
0
20
40
60
80
100
400
600
800

Figure 6

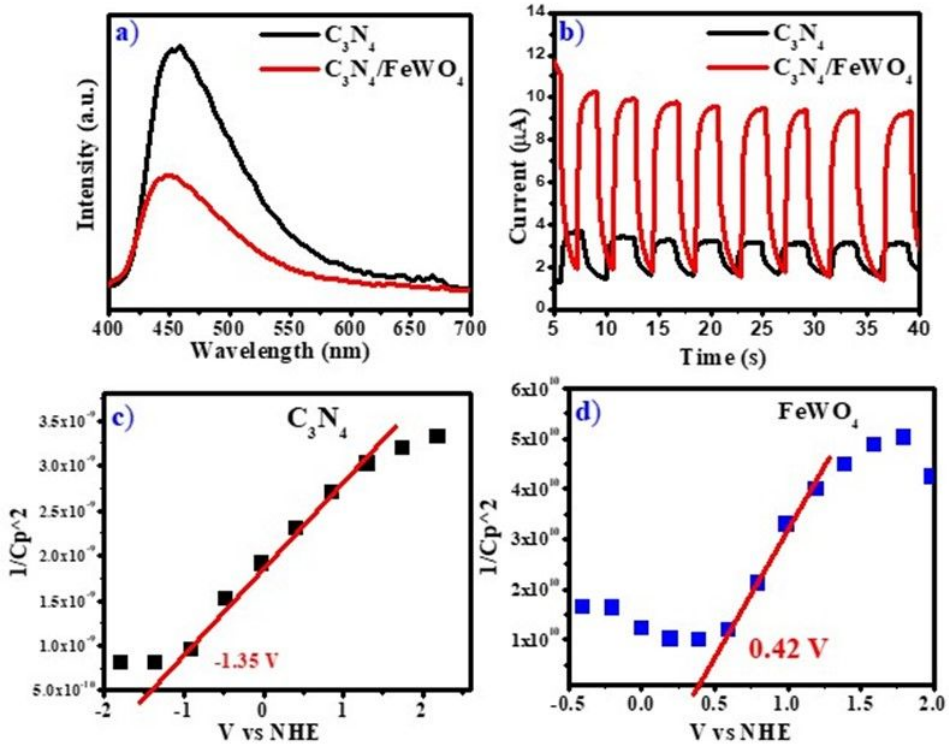
a)
C_3N_4
$C_3N_4/FeWO_4$
Intensity (a.u.)
Wavelength (nm)
b)
C_3N_4
$C_3N_4/FeWO_4$
Current (μA)
Time (s)
c)
C_3N_4
-1.35 V
1/Cp^2
V vs NHE
d)
$FeWO_4$
0.42 V
1/Cp^2
V vs NHE

Figure 7

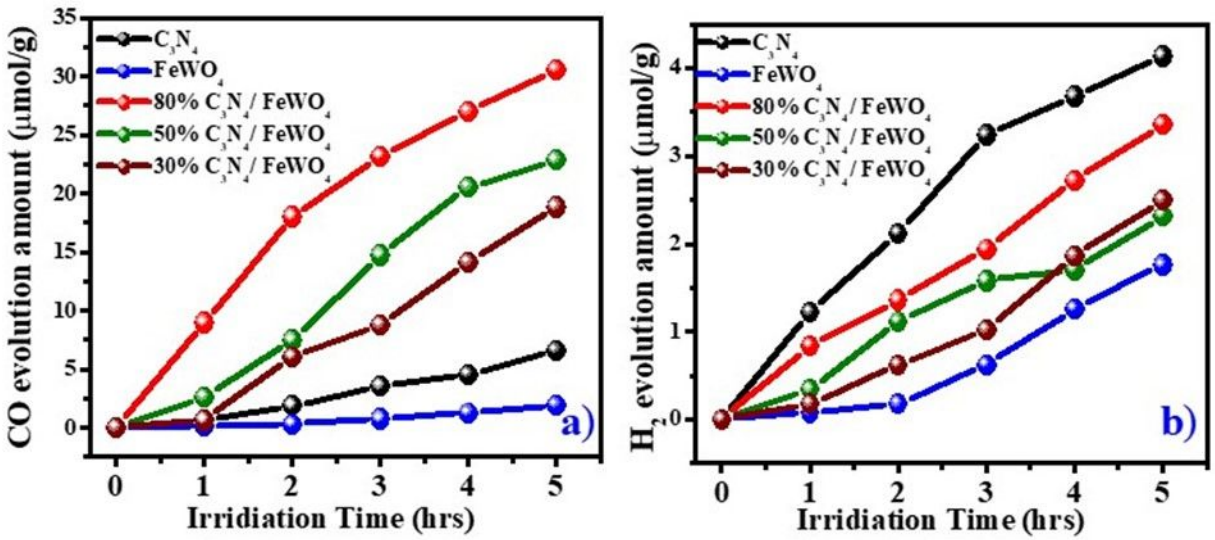
CO evolution amount (μmol/g)
Irridiation Time (hrs)
C3N4
FeWO4
80% C3N4 / FeWO4
50% C3N4 / FeWO4
30% C3N4 / FeWO4
a)
H2 evolution amount (μmol/g)
Irridiation Time (hrs)
b)

Figure 8

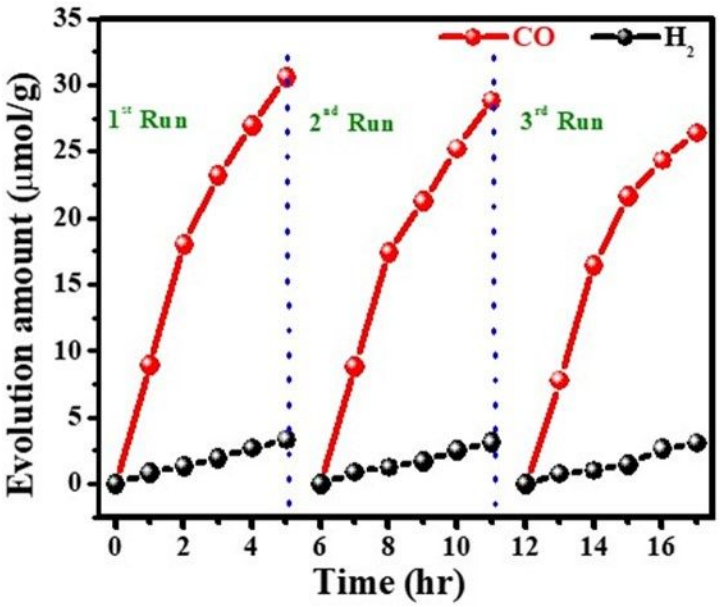
CO
H2
1st Run
2nd Run
3rd Run
Evolution amount (μmol/g)
Time (hr)
0
5
10
15
20
25
30
35
0
2
4
6
8
10
12
14
16

Figure 9

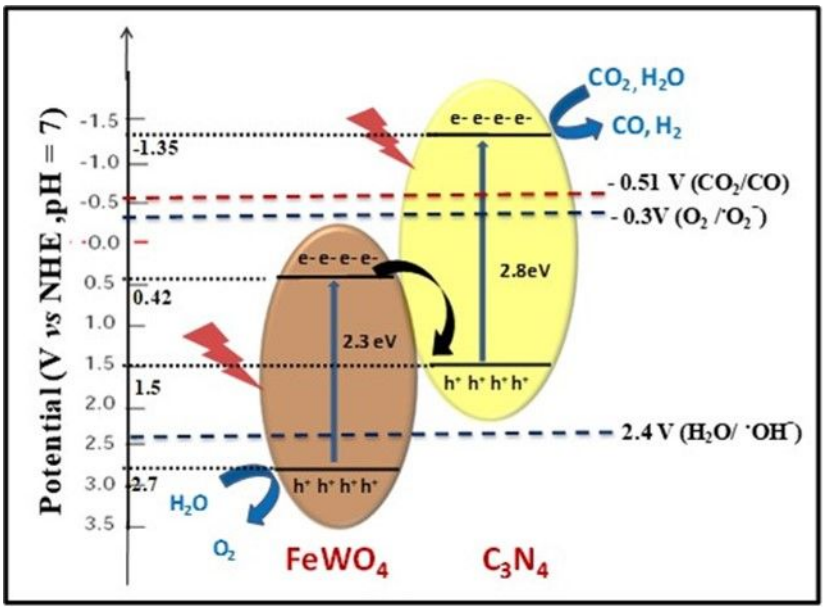
Potential (V vs NHE ,pH = 7)
-1.5
-1.0
-0.5
-0.0
0.5
1.0
1.5
2.0
2.5
3.0
3.5
-1.35
0.42
1.5
-2.7
e- e- e- e-
e- e- e- e-
h+ h+ h+ h+
h+ h+ h+ h+
2.8eV
2.3 eV
CO2, H2O
CO, H2
- 0.51 V (CO2/CO)
- 0.3V (O2 /•O2-)
2.4 V (H2O/ •OH-)
H2O
O2
FeWO4
C3N4

Figure 10

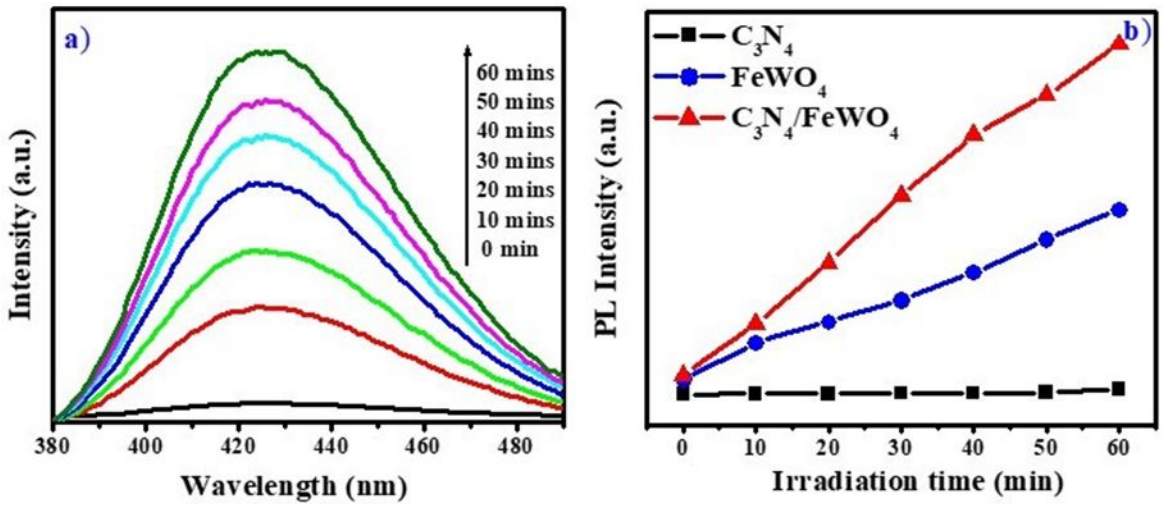
a)
60 mins
50 mins
40 mins
30 mins
20 mins
10 mins
0 min
Intensity (a.u.)
380
400
420
440
460
480
Wavelength (nm)
b)
C_3N_4
$FeWO_4$
$C_3N_4/FeWO_4$
PL Intensity (a.u.)
0
10
20
30
40
50
60
Irradiation time (min)

SYNOPSIS:

An efficient direct Z scheme photocatalyst $FeWO_4/C_3N_4$ for selective CO_2 photoreduction to CO

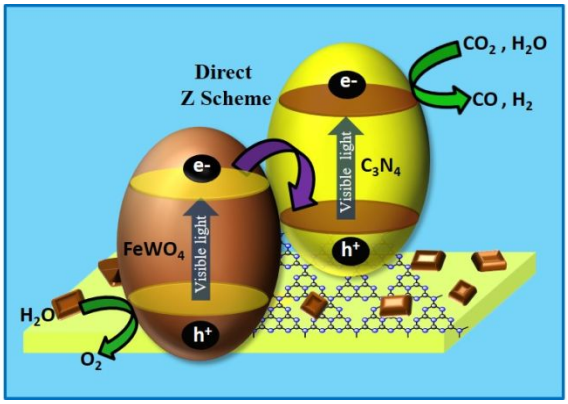

TOC Figure